Applied Catalysis B: Environmental 307 (2022) 121203

Contents lists available at ScienceDirect

Applied Catalysis B: Environmental

journal homepage: www.elsevier.com/locate/apcatb

Construction of Pt-mTiO$_2$/USY multifunctional catalyst enriched with oxygen vacancies for the enhanced light-driven photothermocatalytic degradation of toluene

Ehiaghe Agbovhimen Elimian [a,b,1], Meng Zhang [a,c,e,1], Jing Chen [d,e], Hongpeng Jia [a,c,e,*], Yong Sun [b], Jun He [b]

[a] Xiamen Key Laboratory of Materials for Gaseous Pollutant Control, Institute of Urban Environment, Chinese Academy of Sciences, Xiamen 361021, China
[b] Department of Chemical and Environmental Engineering, Faculty of Science and Engineering, University of Nottingham, Ningbo 315100, China
[c] CAS Center for Excellence in Regional Atmospheric Environment, Chinese Academy of Sciences, Xiamen 361021, China
[d] Xiamen Institute of Rare-earth Materials, Haixi Institutes, Chinese Academy of Sciences, Xiamen 361021, China
[e] University of Chinese Academy of Sciences, Beijing 100049, China

ARTICLE INFO

Keywords:
TiO$_2$-based catalyst
USY zeolite
Light-driven thermocatalysis
Oxygen vacancies
Photoactivation

ABSTRACT

Light-driven thermocatalysis has emerged as an attractive approach for catalytic oxidation of volatile organic compounds (VOCs). Herein, we have synthesized Pt-mTiO$_2$/USY nanocomposites for the catalytic degradation of toluene under full solar spectrum. The mTiO$_2$/USY with increasing Pt content show increased activity, among which 0.9Pt-mTiO$_2$ exhibits toluene conversion of 86.6% and CO$_2$ yield of 74.5% at 243 °C with a light intensity of 490 mW/cm^2 under 5 vol.% water vapor. The high catalytic performance of Pt-mTiO$_2$/USY can be attributed to the large surface area, strong light absorption, highly efficient conversion of light-to-heat, abundant oxygen vacancies, uniform Pt distribution, and Ti^{3+} species on the catalyst surface. The introduction of Pt nanoparticles (NPs) in mTiO$_2$/USY enhances light absorption and improves the mobility of surface lattice oxygen. The combination of EPR, O$_2$-TPD, and in situ DRIFTS analysis reveals that light irradiation further stimulates more active lattice oxygen to participate in the toluene oxidation.

1. Introduction

Volatile organic compounds (VOCs) are major precursors of atmospheric pollutants, which are detrimental to human health and the environment. Thus, the development of efficient VOCs elimination is urgently needed [1]. Catalytic oxidation is considered an efficient technology for the degradation of VOCs to less harmful byproducts (CO$_2$ and H$_2$O). Notwithstanding the merits, the operation process is very costly and dependent on nonrenewable energy sources to achieve operating temperature [2]. In addition, the presence of water vapor, a typical component of industrial waste gas, reportedly suppresses the catalyst activity by binding strongly to the surface active sites [3,4]. Solar radiation represents a renewable source of energy, notwithstanding the solar-driven photocatalytic oxidation of refractory VOCs are characterized by low conversion efficiency due to rapid recombination of charge carriers and poor utilization of solar irradiation [1,5]. Most recently, light-driven thermocatalysis has emerged as a strategy that permits greater exploitation of the solar spectrum for the oxidation of VOCs as compared to conventional photocatalytic oxidation and eliminates the energy consumption of the catalytic oxidation process. Previous research has established that both non-radiative heat and reactive radicals are necessary for the promotion of catalytic reactions [6]. It is also found that light-driven thermocatalysis based on transition metal oxides is often accompanied with the photoactivation of surface oxygen species [7]. Despite the merits, the development of high-performance durable catalysts and the elucidation of the actual reaction mechanism during light-driven thermocatalysis oxidation remain challenging.

Titanium dioxide (TiO$_2$) nanomaterial, as a promising candidate for light-driven thermocatalysis, have been widely applied in the field of

* Corresponding author at: Xiamen Key Laboratory of Materials for Gaseous Pollutant Control, Institute of Urban Environment, Chinese Academy of Sciences, Xiamen 361021, China.
E-mail address: hpjia@iue.ac.cn (H. Jia).
[1] Contributed equally to this work.

https://doi.org/10.1016/j.apcatb.2022.121203
Received 27 October 2021; Received in revised form 15 January 2022; Accepted 8 February 2022
Available online 10 February 2022

environment pollution removal. The light absorption is limited by the large bandgap between 3.0 and 3.2 eV which further affects its catalytic performance. Surface defect engineering can improve the light absorption properties of materials. For example, the hydrogenation of TiO_2 can prepare defective TiO_{2-x} with the presence of abundant oxygen vacancies (OVs) and Ti^{3+} species, which extends the light absorption of TiO_2 to the visible light region [8,9]. The positively charged OVs on metal oxides not only promote the separation of photogenerated electron-charge carriers but also serve as active sites for toluene activation and thermodynamically accelerate the conversion of activated toluene [8,10,11]. Even so, the high agglomeration tendency associated with TiO_2 nanoparticles (NPs) still limits the practical application. The introduction of noble metals to the surface of TiO_2 can increase the light absorption of visible and near-infrared (NIR) spectrum and simultaneously act as active sites for enhancing the deep oxidation of VOCs during the reaction. Despite the associated merits, the low surface area and narrow pore volumes of transition metal oxides as supports reduce the overall efficiency of the catalyst [12,13]. Therefore, the nature of the catalyst support plays an important role in the degradation of organic pollutants.

A variety of support materials have been explored for the degradation of environmental pollutants (e.g., Al_2O_3, MnO_2, TiO_2, carbon, reduced graphene)[6,7,14–16]. From the point of material design, nanomaterials with a large specific area and strong adsorption capacity of the reactants are highly desirable. In our group, for example, the strong deactivation of 1% Pt-TiO_2 was observed and attributed to the accumulation of incomplete oxidation of intermediates during the oxidation of toluene, while Pt supported on rGO-TiO_2 showed remarkable photothermal catalytic activity under IR irradiation for oxidation of toluene [14]. They concluded that enhanced activity was due to the strong light-to-heat conversion and the high adsorption of reactant molecules, as well as the good dispersion supported Pt–TiO_2 catalyst on the rGO nanosheets [16]. Recently, zeolites are being actively studied as support for photoactive catalysts capable of solar energy conversion. Zeolites have been proven useful in assisting charge separation by hindering energy-wasting back electron transfer and the stabilization of photo-induced electrons [17,18]. These microporous materials are being considered as excellent catalyst support materials for practical elimination VOCs due to the large specific surface area, intricate channels, and excellent thermal stability (600 °C in the air) [19]. The large specific surface area prevents the aggregation of the active site of NPs and the owned abundant Lewis acidic sites can also promote the adsorption of VOCs molecules, which are advantageous to catalytic oxidation reaction [19,20]. The ultra-stable Y (USY) zeolite with faujasite topology is very stable and suitable for the efficient adsorption of toluene from humid air streams compared to other faujasite zeolites such as NaY and NaX [21]. Also, the large specific surface area of USY could promote the dispersion of TiO_2 and Pt species [22].

With a view to the synergistic effect of different components, we synthesized xPt-mTiO_2/USY nanocomposites by combining ultra-stable Y (USY), TiO_2 and Pt, and studied the light-driven catalytic oxidation of toluene over these catalysts. The 0.9Pt-mTiO_2/USY exhibits high catalytic performance with 88% of toluene conversion and 74% of CO_2 yield under simulated solar light irradiation with an intensity of 460 mW/cm^2, along with good photothermal catalytic stability at least for five runs. The comparative characterizations confirm that the better light-driven thermocatalytic activity is derived from the synergistic effects of strong light absorption, efficient light-to-heat conversion, enhanced lattice oxygen mobility and toluene adsorption, more oxygen vacancy defects, and highly active Pt catalytic sites. It also strongly suggests that light illumination stimulates the activation of more lattice oxygen and accelerates the degradation of toluene. The metallic Pt nanoparticles and oxygen vacancies act as active sites for the activation of molecular O_2 whereas the USY offers sites for the adsorption of toluene and desorption of CO_2 and H_2O. Moreover, the Pt-mTiO_2/USY catalysts also exhibited favorable catalytic activity for other VOCs, such as benzene, ethyl acetates and formaldehyde under humid conditions. This work highlights the exploration of Pt-TiO_2 zeolite-based nanomaterial as a solar light energy converter for catalytic oxidation of recalcitrant VOCs.

2. Experimental section

2.1. Materials

Titanium tetraisopropoxide (95%), Ethanol Absolute (99.7%), USY zeolite (SiO_2/Al_2O_3 ratio of 5:4), Hexachloroplatinic(IV) acid hexahydrate (H_2PtCl_6,), Polyvinylpyrrolidone K30 (PVP, 99%, Mr 40000), Hexadecylamine (HDA) surfactants Ethylene glycol (99.5%). All chemicals used were A.R. grade without further purification and were purchased from Sinopharm Chemical Reagent Co., Ltd.

2.2. Catalyst preparation

2.2.1. mTiO$_2$/USY

First, 1.0 g of USY was dispersed in 2 wt.% polyvinyl pyrrolidone (PVP) solution and stirred for 12 h at room temperature. The products were separated by centrifugation, washed three times with water, and then dried at 80 °C in a vacuum oven overnight. And then the obtained samples were calcinated at 400 °C for 1 h with a heating rate of 2 °C/min in N_2 to gain USY/PVP nanocomposite. The USY/PVP powder was homogeneously dispersed in the solution of ethanol and ethylene glycol by ultrasonication and subsequently, 0.08 g of 1-hexadecylamine (HDA) surfactant was added. The detailed procedure for the uniform coating of NPs with titanium dioxide has previously been reported [24]. 4 mL of titanium tetra-isopropoxide (TTIP) was added into the above solution and stirred for 3 h at room temperature. The theoretical amount of titanium ions was determined to be 50 wt%. The resulting suspension was filtrated, washed thoroughly with water and ethanol, dried at 100 °C, and finally calcined at 400 °C for 4 h in air to obtain mTiO_2/USY.

2.2.2. xPt-mTiO$_2$/USY

The xPt-mTiO_2/USY catalysts were prepared via wet impregnation of Pt species. Typically, the as synthesized mTiO_2/USY was dispersed in a 50 mL solution containing ethanol and stoichiometric amounts of an aqueous solution of H_2PtCl_6 (3.8 g/L). The samples were stirred at 80 °C until the water was vaporized. The mixture was dried in an oven at 120 °C for 4 h and calcinated at 400 °C for 4 h in air. The obtained catalysts were donated as 0.4Pt-mTiO_2/USY, 0.6Pt-mTiO_2/USY and 0.9Pt-mTiO_2/USY according to Pt loading contents of 0.43, 0.62 and 0.93 wt.% (Table 1), respectively. For comparison, the preparation procedure of mesoporous TiO_2 (mTiO_2) and 0.9Pt-mTiO_2 (Pt loading content of 0.90 wt.%) was similar to mTiO_2/USY and xPt-mTiO_2/USY without the addition of USY zeolite. All synthesized samples were reduced via treatment under H_2 flow (100 mL/min) at 600 °C for 3 h with a heating rate of 2 °C/min.

2.3. Characterization

Powder X-ray diffraction (XRD) was conducted on an X′Pert Pro automatic powder diffractometer with Cu Kα monochromatized radiation. Scanning electron microscopy (SEM) image and energy dispersive X-ray spectroscopy (EDX) mapping of the elements were obtained on Oxford XMAS 80 T. Transmission electronic microscopy (TEM) was performed on JEM 2100 EX instrument. Nitrogen adsorption-desorption measurements of the catalysts were performed on a Quantachrome autosorb iQ2 adsorption automatic instrument at liquid nitrogen temperature. All samples were degassed under vacuum at 60 °C for 24 h before the measurement. The specific surface area and pore volume of the catalyst were calculated from the nitrogen adsorption-desorption isotherms using the Brunauer-Emmett-Teller (BET) and Barrett-Joyner-Halenda (BJH) methods. The UV–Vis-IR absorption spectra were

Table 1
Physiochemical properties of different catalysts.

Sample	S_{BET} (m^2/g)	Total pore volume (cm^3/g)	Micropore volume (cm^3/g)[a]	Average pore size (nm)[b]	Pt loading (wt.%)[c]	O_{ads}/ (O_{latt}+O_{H2O})[d]
USY	700	0.34	0.32	2.4	_	
$mTiO_2$/USY	502.2	0.25	0.15	3.4	_	0.32
0.4Pt-$mTiO_2$/USY	498.7	0.27	0.18	2.3	0.43	0.34
0.6Pt-$mTiO_2$/USY	492.2	0.29	0.20	2.3	0.62	0.36
0.9Pt-$mTiO_2$/USY	487.6	0.31	0.22	2.3	0.93	0.37
1.1Pt-$mTiO_2$/USY	482.3	0.32	0.22	2.3	1.08	0.38
0.9Pt-$mTiO_2$	46.5	0.14	_	9.07	0.90	_
$mTiO_2$	47.9	0.16	_	9.06	_	_

[a] Estimated at $P/P_o = 0.95$.
[b] *t*-plot.
[c] Measured by ICP-OES.
[d] Obtained from the XPS results.

recorded using a Shimadzu UV-2550 spectrophotometer in the 200 – 2500 nm range at room temperature. The $BaSO_4$ was used as a reference to inspect the optical property of the sample. XPS analysis was conducted on a Kratos AXIS Supra using monochromatic Al Kα radiation (1486.6 eV) as the X-ray source operated at 150 W. The pressure in the main chamber was maintained at approximately 10^{-9} torr during the analysis. Raman spectroscopy was carried out on LabRAM Aramis using a green laser of 532 nm wavelength. The actual loading content of noble metal was determined by inductively coupled plasma atomic emission spectroscopy (ICP-OES, PerkinElmer Optima 7000DV). Oxygen temperature programmed desorption (O_2-TPD) measurement was performed on a Quantachrome Chemstar instrument. 30 mg catalyst sample was filled in a vessel and pretreated in a He flow (50 mL/min) at 350 °C for 60 min then cooled to 35 °C and kept at this temperature for 60 min in a flow of 5 vol.% O_2/He (30 mL/min). Then, the gas pipeline was swept with He for 120 min, and the sample was heated to 900 °C at a rate of 10 °C/min in a Helium flow of 30 mL/min. Toluene temperature programmed desorption (toluene-TPD) was performed on a ChemStar chemisorption analyzer equipped with a thermal conductivity detector. 100 mg of the catalyst was placed in a quartz tube and purged by pure He at 350 °C for 1 h and cooled to 40 °C before the adsorption of toluene for 1 h. After saturation with toluene, the sample was again flushed with pure He for 1 h at 40 °C. Then toluene signals were recorded online from 40° to 400°C at a rate of 10 °C/min. Electron paramagnetic resonance (EPR) spectra were obtained from Bruker A300 spectrometer at 77 K. *In situ* diffuse reflectance infrared Fourier transform spectroscopy (*In situ* DRIFTS) was performed on an FTIR spectrometer (Nicolet Nexus 670) equipped with a smart collector and MCT/A detector. Prior to the experiment, the sample was pretreated at 350 °C for 1 h in a He flow to remove adsorbed impurities. Thereafter, 200 ppm toluene/He flow into the cell at a rate of 30 mL/min at room temperature. Subsequent experimental details will be given in the corresponding results and discussion section.

2.4. Light-driven catalytic activity

The catalytic activity for gaseous toluene oxidation over samples was examined in a cylindrical stainless-steel reactor with a quartz window. A 300 W xenon lamp (PLS-SXE300/300UV, Perfect Light) and an infrared (IR) lamp (PHILIPS IR 375 CH IR2) were used as the sources of solar light. To measure the catalytic activity driven by ultraviolet−visible (UV-Vis) or IR light, the appropriate cut-off filter was placed between the lamp and the quartz window of the reactor. The light intensity of the xenon lamp used on the catalysts was 460 mW/cm^2 measured by an optical power meter (CEL-NP2000-2). Before the catalytic test, 30 mg of catalyst was dispersed in ethanol, then coated on a fiberglass-membrane of 50 mm diameter by filtration and dried at 80 °C. An aluminum silicate fiber was also placed at the bottom of the reactor to decrease the loss of energy. A thermocouple was placed at the center of the catalyst layer to measure the change in the surface temperature under illumination. Prior to irradiation, the adsorption-desorption equilibrium of toluene on the catalyst was performed in the dark. A feed gas containing 200 ppm toluene was generated by bubbling 21% O_2/N_2 through liquid toluene, then passed through the catalyst at a flow rate of 13 mL•min^{-1}, giving a gas hourly space velocity (GHSV) of 26000 mL•g^{-1}•h^{-1}. The humid condition was generated by introducing 5 vol.% H_2O vapor into the feed stream through a water saturator at a specific temperature. The amount of reactant and product were determined by a GC 9160 gas chromatograph (GC) equipped with a flame ionization detector (FID) and a thermal conductivity detector (TCD).

The toluene conversion and CO_2 yield were calculated by the following equations:

$$Toluene\ \ conversion\ \ = \ \ \frac{[Toluene\ \ ]_{in} - [Toluene\ \ ]_{out}}{[Toluene]_{in}} \ \ \times \ \ 100\% \tag{1}$$

$$CO_2\ \ yield\ \ (\%) \ \ = \ \ \frac{[CO_2]_{produced}}{[CO_2]_{theoretical}} \ \ \times \ \ 100\% \tag{2}$$

3. Results and discussion

3.1. Catalyst synthesis strategy

The sol-gel synthesis route using a glycosylated precursor such as ethylene glycol has proven to be an effective synthesis method for the synthesis of TiO_2-based nanocomposite, although limitations such as poor control of size distribution and shape variation and large particle aggregation still exist. To improve reproducibility and reduce the aggregation of the particles, we report a versatile surfactant-mediated sol-gel strategy for the synthesis of supported Pt-$mTiO_2$/USY nanocomposite as illustrated in Fig. S1 [23,24]. The USY/PVP powder was homogeneously dispersed in ethanol and ethylene glycol by ultrasonication, followed by the addition of hexadecyl amine (HDA) surfactants under stirring. The HDA molecules segregate to the surface of the USY. With the addition of titanium ions into the precursor titanium tetra-isopropoxide, the titanium ions react with ethylene glycol and ethanol to form a titanium glycolate, which reduces the rate of hydrolysis of TTIP [24,25]. The titanium glycolate is highly stable in alcohol and humid atmosphere[24,26]. Meanwhile, on the surface of the USY zeolite, the hydrogen bonding interaction between the amine group of the HDA molecules and the titanium glycolate occurs on the surface of the USY to form an inorganic-organic bond that reduces the formation of large TiO_2 aggregation and improves size uniformity[23]. The Pt NPs were introduced to the surface of the $mTiO_2$/USY surface by the wet impregnation method. Moreover, the TiO_2 and platinum oxide supported on the USY zeolite were reduced to form oxygen vacancies (Ov), Ti^{3+} species metallic Pt particles by hydrogen treatment as shown in Eqs. 1,2, and 3 [27,28].

$$O_o^x \leftrightarrow O_v + 2e^{'} + 1/2O_2 \tag{1}$$

$$Ti^{4+} + 2O_o^x \leftrightarrow Ti^{3+} + 3e' + O_2 \quad (2)$$

$$PtO_2 + 2H_2 \rightarrow Pt^0 + H_2O \quad (3)$$

where: O_o^x is the O^{2-} ion in the oxygen lattice site, O_v is oxygen vacancy, e' is the Ti^{3+} ion in the titanium lattice site (quasi-free electron).

Therefore, this synthetic strategy can be potentially utilized in synthesizing highly dispersed Pt NPs supported on USY zeolite.

3.2. Characterization

XRD patterns of samples, as shown in Fig. 1**a,** are in good agreement with the standard data of USY, where the diffraction peaks located at 23.3° and 26.6° correspond to the (533) and (642) crystal planes of USY [30]. The XRD patterns confirm that the structure of USY remains unaltered for all samples after calcination and hydrogenation. The peaks found at 25.6°, 38.1°, and 48.4° correspond to the diffractions from (101), (004) and (200) planes of anatase TiO_2 (JCPDS no. 01–084–1286), and the diffraction peaks located at 27.4°, 36.0°, and 41.2° attribute to the crystal planes (110), (101), and (111) of rutile TiO_2 (JCPDS no. 01–075–1753) [31]. No distinctive peaks corresponding to the oxide or metal state of Pt are observed in the xPt-mTiO$_2$/USY samples even with 1.1% Pt loading, which can be reasonably ascribed to the low content of Pt loading or high dispersion of small-size Pt NPs. Raman spectra of samples were performed to acquire more structural information, as shown in Fig. 1**b**. For all samples, only vibration bands of TiO_2 are identified, where the bands at 143 cm^{-1} (E_g), 198 cm^{-1} (E_g), 396 cm^{-1} ($B_{1\,g}$), 516 cm^{-1} ($A1_g$ + $B1_g$), and 637 cm^{-1} (E_g) are from anatase TiO_2 and the band at 440 cm^{-1} (E_g) is a typical peak of rutile TiO_2 [32]. The Raman result is in accordance with the XRD analysis as mentioned above. Moreover, the blue shift of TiO_2 anatase peak toward a high wavenumber from 143 cm^{-1} to 147 cm^{-1} for 0.9Pt-mTiO$_2$/USY and 1.1Pt-mTiO$_2$/USY indicating the symmetric stretching vibration of O-Ti-O in TiO_2 is partially destroyed due to the strong interaction between Pt and TiO_2 [14].

N_2 adsorption-desorption isotherms of all USY supported samples exhibit a IV-type isotherm with two hysteresis loops at low (<0.1 P/P_0) and medium (0.2–0.9 P/P_0), which is typical of microporous materials mixed with a certain degree of mesoporosity [33]. The mTiO$_2$ and 0.9Pt-mTiO$_2$ samples show the type III isotherm features with an H3 hysteresis loop (Fig. S2). As listed in Table 1, the values of S_{BET} are decreased with increasing Pt loading. The reduction of the surface area indicates that the introduction of TiO_2 particles fills in the porous channel of USY. The pore volume of the mTiO$_2$/USY support was observed to increase with the loading of Pt NPs, which can be ascribed to the formation of new channels within the USY framework. In addition, the obtained xPt-mTiO$_2$/USY samples inherit the characteristics of the large S_{BET} (ca. 498–482 m^2/g) from USY, which is helpful to increase the exposed active surface sites for the adsorption and activation of reactant molecules.

The SEM images of mTiO$_2$/USY and xPt-mTiO$_2$/USY also show the octahedral morphology of USY (Fig. S3), although the surface becomes rougher with the increasing addition of TiO_2 and Pt NPs. The presence of TiO_2 on the surface of USY was observed with the lattice spacing of ca. 0.352 nm and 0.230 nm corresponding to the (101) and (004) planes of the TiO_2 anatase phase obviously appears in HRTEM images (Fig. 2**a-c**) [23]. For the optimized 0.9Pt-mTiO$_2$/USY, TEM images (Fig. 2**d** and **e**) clearly show the uniform distribution of Pt NPs (~ 2.7 nm of size) on the surface of mTiO$_2$/USY. The HRTEM image of 0.9Pt-mTiO$_2$/USY (Fig. 2**f**) also displays the lattice spacing of 0.235 nm from the Pt (111) besides the lattice spacing of TiO_2, which confirms the successful loading of Pt species [34]. HAADF-STEM image and the EDX elemental mapping of 0.9Pt-mTiO$_2$/USY verify the uniform dispersion of Ti and Pt elements, as shown in Fig. 2**g**. The large surface area and the extra-framework Al-OH or Si-OH groups of USY enhance the hybridization of Ti species and dispersion of Pt NPs on the surface. Hydrogen treatment further modulates the electronic structure of Pt and creates more surface OVs on 0.9Pt-mTiO$_2$/USY that can promote the activation of adsorbed toluene to boost the catalytic activity [35,36]. At the same time, the uniform exposure of Pt NPs on the surface of USY facilitates the capture and utilization of photons in the longer wavelength range.

The high-resolution Ti 2p XPS spectrum of the catalyst is shown in Fig. 3**a**. For all samples, the Ti 2p XPS peak is fitted by four components with the binding energies at 464.7, 463.8, 458.9, and 458.0 eV, which are attributed to Ti^{4+} $2p_{1/2}$, Ti^{3+} $2p_{1/2}$, Ti^{4+} $2p_{3/2}$ and Ti^{3+} $2p_{3/2}$, respectively, confirming the formation of Ti^{3+} ions in the TiO_2 lattice through hydrogenation [37]. The three fitted O 1 s XPS peaks (Fig. 3**b**) observed around 529.4, 530.5, and 532.3 eV can be assigned to lattice oxygen (O_{latt}), absorbed oxygen (O_{ads}), and oxygen species in surface-absorbed water (OH_2O), respectively. The ratio of $O_{ads}/(O_{latt}+OH_2O)$ for xPt-mTiO$_2$/USY samples is gradually enhanced with increasing Pt loading on mTiO$_2$/USY, and 1.1Pt-mTiO$_2$/USY possesses the highest value. It is commonly considered that the ratio of $O_{ads}/(O_{latt}+OH_2O)$ is tightly related to OVs and the higher ratio leads to a high concentration of OVs [36]. Thus, it declares that 1.1Pt-mTiO$_2$/USY has the most OVs. It is also verified by EPR studies of mTiO$_2$/USY and xPt-mTiO$_2$/USY (Fig. S4), where the signal intensities of OVs and Ti^{3+} are raised with the content of Pt loading and 1.1Pt-mTiO$_2$/USY with the highest Pt amount exhibits the strongest signal. The presence of OVs in the nonstoichiometric semiconductor enhances the adsorption and activation of reactant molecules. Taking into account the peak overlaps

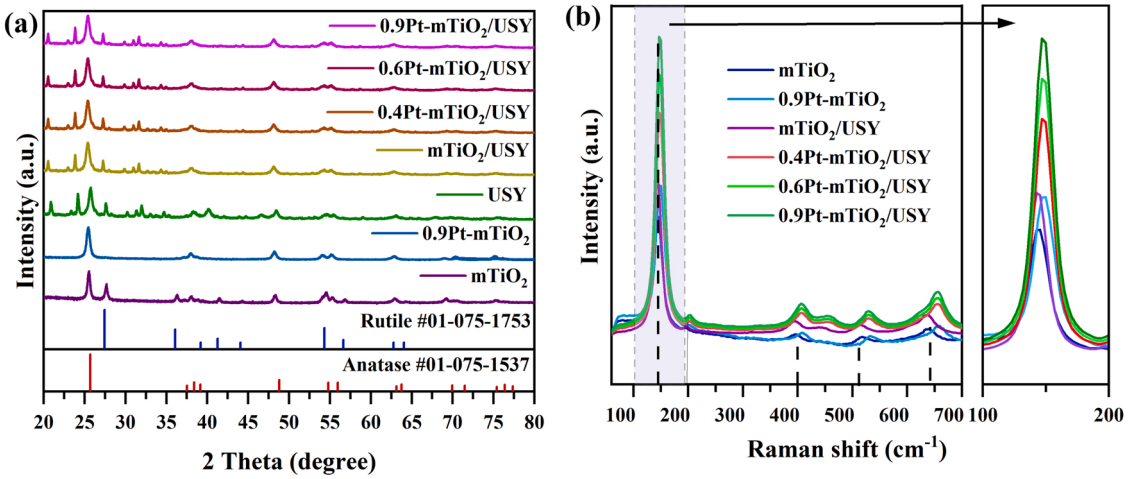

Fig. 1. XRD patterns (a) and Raman spectra (b) of all samples.

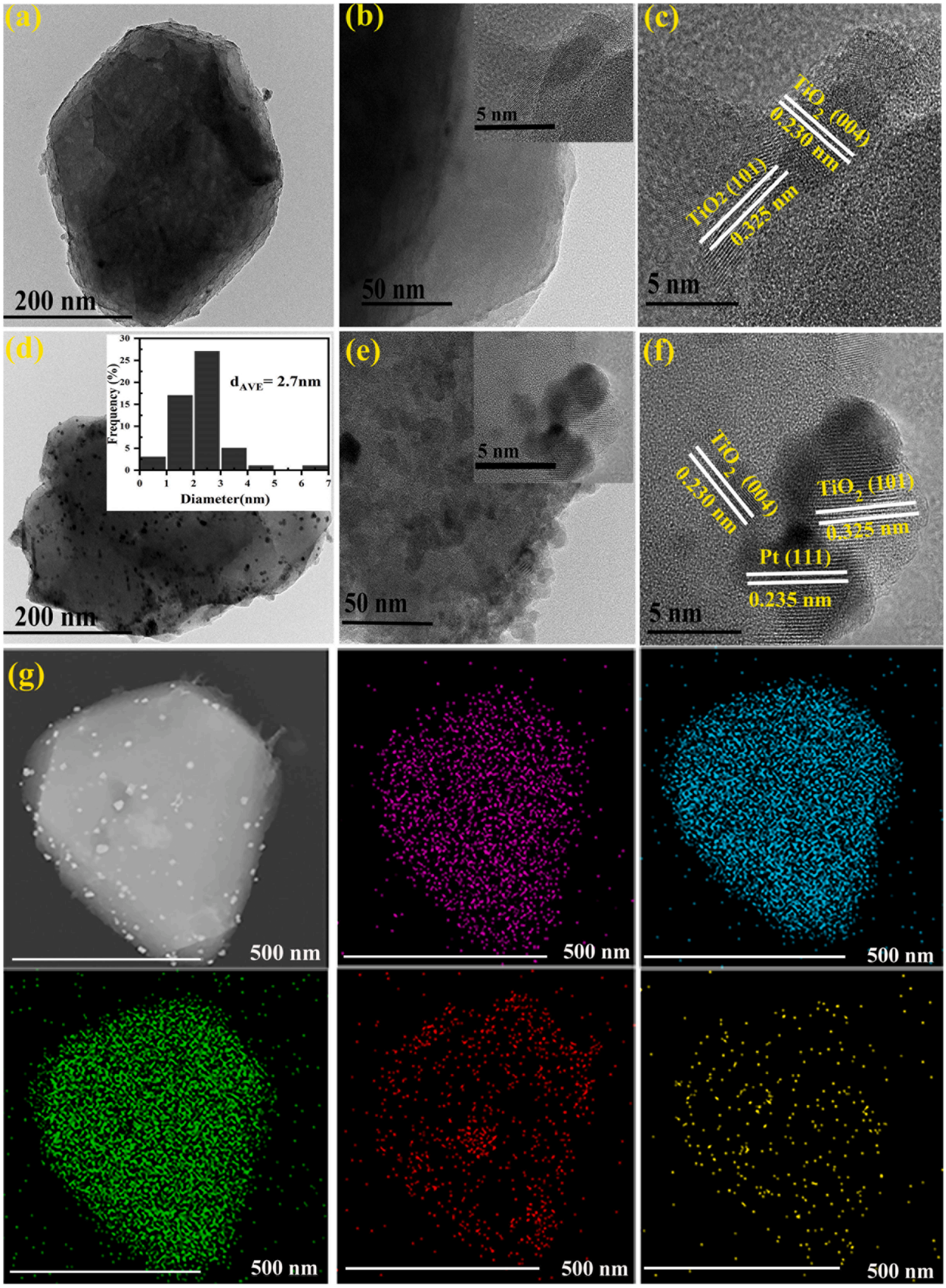

Fig. 2. HRTEM images of $mTiO_2$/USY (a-c) and 0.9Pt-$mTiO_2$/USY (d-f) (insert the corresponding the high-resolution TEM shots of the selected area in the panel); HAADF-STEM image and TEM-EDX elemental mapping of Al, Si, O, Ti, and Pt distribution of 0.9Pt-$mTiO_2$/USY (g).

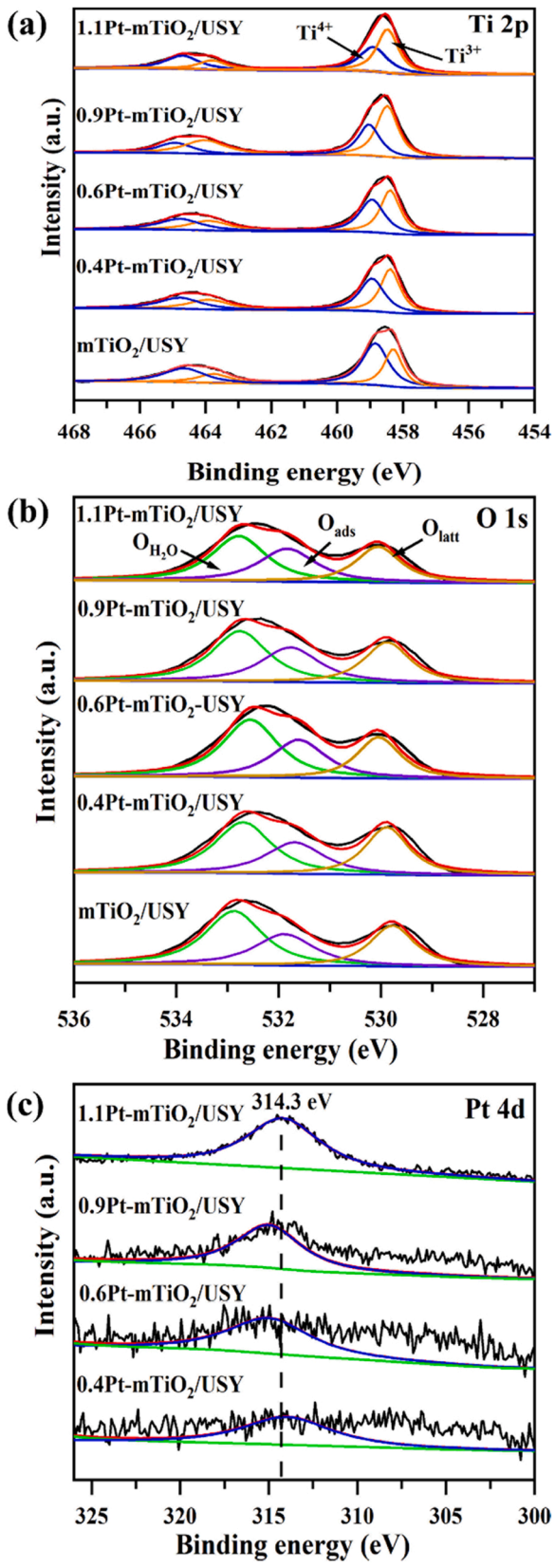

Fig. 3. XPS spectra of Ti 2p (a), O 1s (b), and Pt 4d (c) of $mTiO_2$/USY, 0.4Pt-$mTiO_2$/USY, 0.6Pt-$mTiO_2$/USY, 0.9Pt-$mTiO_2$/USY and 1.1Pt-$mTiO_2$/USY.

of Al 2p and Pt 4 f, Pt 4d is selected to analyze the chemical state of Pt. Even though the intensity of Pt 4d peak is weak, a characteristic peak of metallic Pt at 314.3 eV in Pt 4d spectra is still presented for all xPt-$mTiO_2$/USY samples (Fig. 3**c**), which is due to the complete reduction of oxidized Pt to metallic Pt [38]. The metallic Pt (Pt^0) species have been identified as catalytic active sites for the activation and oxidation of toluene [36]. The results of XPS analysis indicate the introduction of Ti^{3+} species, OVs, and metallic Pt on the catalyst surface via hydrogen treatment at 600 °C.

3.3. Light-driven photothermocatalytic activity

The catalytic activities of catalysts were evaluated by investigating toluene degradation under light irradiation with a light intensity of 490 mW/cm^2 by a Xe lamp in the presence of 5 vol.% water vapor. As displayed in Fig. 4**(a) and (b),** toluene degradation on pure $mTiO_2$ and 0.9Pt-$mTiO_2$ achieve 43.3% and 53.2% within 20 min, respectively which rapidly decreases to corresponding 19.02% and 28.7% within 90 min. The decrease in catalyst activity can be attributed to the gradual deactivation of $mTiO_2$ and 0.9Pt-$mTiO_2$ due to the poor adsorption of toluene molecules and the accumulation of carbonous intermediates on the surface active sites [4]. Although the loading of Pt loading $mTiO_2$ can slightly promote the catalytic activity compared to pure $mTiO_2$, its low specific surface area facilitates agglomeration of Pt NPs and further reduces the number of active sites [39]. In clear contrast to the unsupported $mTiO_2$, the $mTiO_2$/USY achieved a toluene conversion and CO_2 yield of 48.0% and 32.5%, respectively and maintained the toluene conversion of 59% during the reaction time. This result manifests that USY as the support can noticeably improve the photothermal catalytic performance, certainly relating to the large surface area, and abundant Lewis acidic sites of USY. Moreover, the hydrophobic nature of USY zeolite favors the adsorption of toluene on zeolites under humid conditions, due to the Si/Al content [22,40]. The introduction of Pt into $mTiO_2$/USY enhances the catalytic activity for toluene oxidation, as observed for xPt-$mTiO_2$/USY. The catalytic activity of 0.4Pt-$mTiO_2$/USY has a tremendous enhancement with toluene conversion of 79.0% and CO_2 yield of 60.4%, and 0.9Pt-$mTiO_2$/USY shows the best photothermal catalytic performance to accomplish toluene conversion of 86.6% and CO_2 yield of 74.5%. Conversely, in the absence of moisture, the 0.9Pt-$mTiO_2$/USY achieved a toluene conversion of 89.0% and a CO_2 yield of 77.4%, indicating that water vapor had a slight inhibiting effect on 0.9Pt-$mTiO_2$/USY as shown in Fig. S5**.** The increase of Pt loading from 0.9 to 1.1 wt.% (1.1Pt-$mTiO_2$/USY) resulted in the increase of toluene conversion and CO_2 yield to 87.6% and 75.3%, which is an increase of less than 2%. However, the high cost and scarcity of the noble metal hinder the large-scale application of the supported Pt catalyst with approximately 1% or more Pt loading [41,42]. Considering the practical application, we still select 0.9Pt-$mTiO_2$/USY catalyst to further explore the photothermal catalytic reaction mechanism.

The significant difference in reaction durability between 0.9Pt-$mTiO_2$ and 0.9Pt-$mTiO_2$/USY can be attributed to the promotional effect of USY. The BET surface area of 0.9Pt-$mTiO_2$/USY is ca. 487.6 m^2/g, which is tremendously higher than 46.5 m^2/g of 0.9Pt-$mTiO_2$ because of the contribution of USY large surface area. Furthermore, the USY efficiently limits the agglomeration of Pt NPs in xPt-$mTiO_2$/USY, which improves the utilization of Pt NPs towards light absorption and reactants adsorption to enhance the catalytic reaction. The application of the USY material as catalyst supports promotes the adsorption-desorption kinetics of reactants thus achieving great enhancement of catalytic performance. The toluene-TPD experiment (Fig. 5) shows that xPt-$mTiO_2$/USY with USY support has a much stronger adsorption capacity towards toluene than $mTiO_2$ and 0.9Pt-$mTiO_2$, which is due to the strong electrostatic interactions between the positively polarized methyl group of toluene and a basic oxygen atom in the zeolite framework. Simultaneously, the adsorption capacity of toluene on xPt-$mTiO_2$/USY is steadily heightened with the rising of Pt loading, with the 1.1Pt-$mTiO_2$/

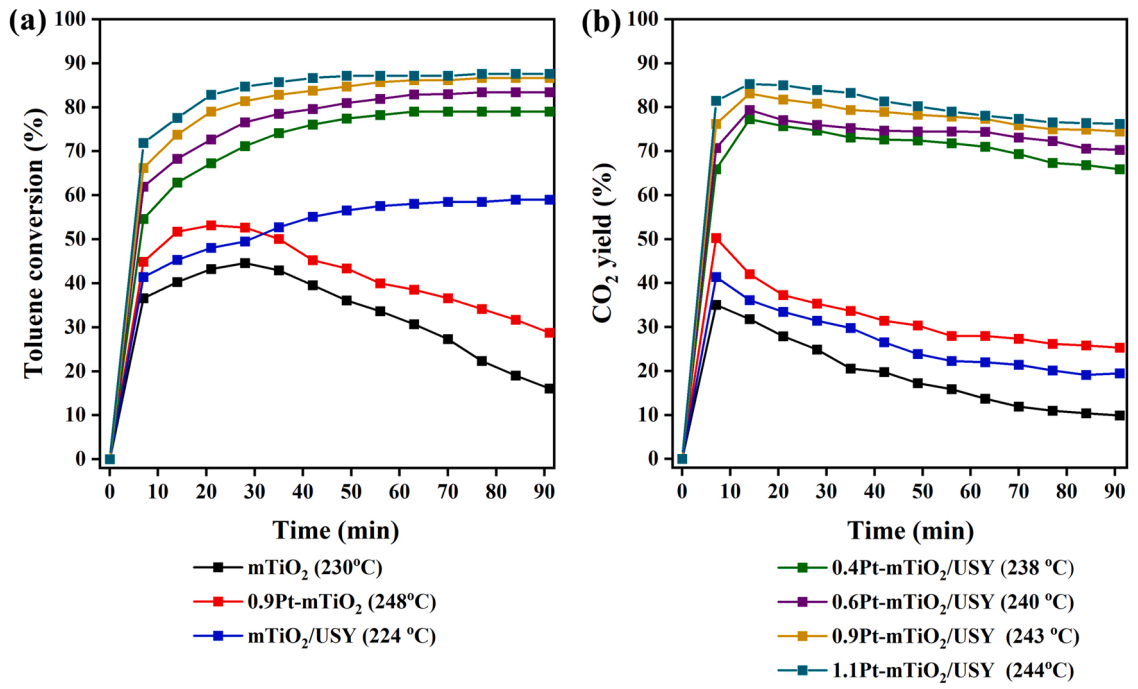

Fig. 4. Toluene conversion (a) and CO_2 yield (b) of the samples for light-driven photothermal catalytic oxidation of toluene under 490 mW/cm^2 of light intensity (200 ppm, 5 vol.% H_2O and WHSV = 26,000 mL g^{-1} h^{-1}).

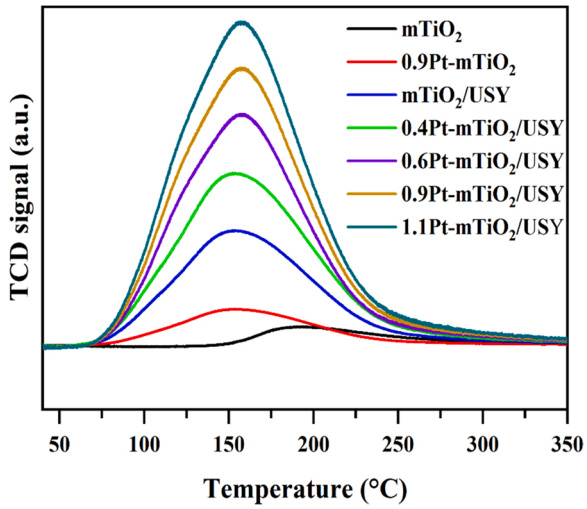

Fig. 5. Toluene-TPD of the samples.

USY displaying the highest toluene adsorption. These phenomena can be ascribed to the increasing concentration of OVs that is conducive to adsorption and activation of toluene [43]. Therefore, based on the preliminary activity investigation of the catalysts, the synergistic effects of high specific surface area, well-dispersed supported Pt-mTiO$_2$, a large amount of exposed active Pt sites and abundant OVs contribute to the excellent performance of xPt-mTiO$_2$/USY.

Previous studies have confirmed that the strong absorption ability over the full solar spectrum range and the conversion of harvested photons into thermal energy are prerequisites for high-efficient light-driven photothermocatalysis [7,14]. To authenticate this speculation, the light absorption and light-to-heat conversion on samples were investigated by diffuse reflectance spectra (DRS) and the monitoring of the surface temperature of the catalyst layer under irradiation. As depicted in Fig. 6**a**, USY has no light absorption in the region of $>$ 400 nm, and mTiO$_2$ displays the obvious light absorption in the region of 400 – 2500 nm. The combination of mTiO$_2$ and USY further improves the light absorption of 400 – 900 nm, as observed for mTiO$_2$/USY. The introduction of metallic Pt can obtain strong absorption in the full solar spectrum, which agrees with reported literature [38]. As observed, xPt-mTiO$_2$/USY shows an enhancement of light absorption from 200 nm to 2500 nm with increasing Pt loading and followed the sequence: 1.1Pt-mTiO$_2$/USY $>$ 0.9Pt-mTiO$_2$/USY $>$ 0.6Pt-mTiO$_2$/USY $>$ 0.4Pt-mTiO$_2$/USY $>$ mTiO$_2$/USY. This is mainly attributed to the formation of more OVs on TiO$_2$ in the hydrogenation process by Pt introduction, which can enhance the solar light absorption [44]. Increasing the concentration of Pt nanoparticles results in the enhanced light absorption ability of the catalyst. This tendency is well accordant with the variation of the surface temperature of catalyst layer on catalysts under the same irradiation (Fig. 6**b**, Table S1), where surface temperature is dependent on the light intensity and is increased with increasing of light intensity. This confirms that catalysts possess the ability to utilize light energy, especially for the IR region, leading to excellent light-to-heat conversion [7].

Light-driven thermocatalytic performance by tuning light intensity was performed on the selected 0.9Pt-mTiO$_2$/USY in the presence of moisture, as shown in Fig. 6**c** and **d**. Under irradiation with a light intensity of 490 mW/cm^2, the conversion and mineralization of toluene over 0.9Pt-mTiO$_2$/USY is maintained at 86% and 74% within 90 min, respectively. However, with decreasing of light intensity from 460 to 200 mW/cm^2, the toluene conversion decreases to 33% whereas CO_2 yield declines to 9% with reaction time. Synchronously, the monitoring of catalyst surface temperature confirms that the variation of temperature is completely reliant on the light intensity, giving the reaction temperature of 243 °C, 240 °C, 227 °C, 213 °C, and 184 °C corresponding to 490, 460, 400, 350, and 200 mW/cm^2, respectively. Similarly, under dry conditions, the toluene conversion and CO_2 yield decreased from 89.0% and 77.4–38.6% and 11% respectively as light intensity decreased from 490 to 200 mW/cm^2, with reaction time as shown in **Fig.S6.** In other words, the difference in catalytic activities on 0.9Pt-mTiO$_2$/USY results from the different surface temperatures of the catalyst layer that are determined by incident light intensities, where the energy supply is based on light-to-heat conversion.

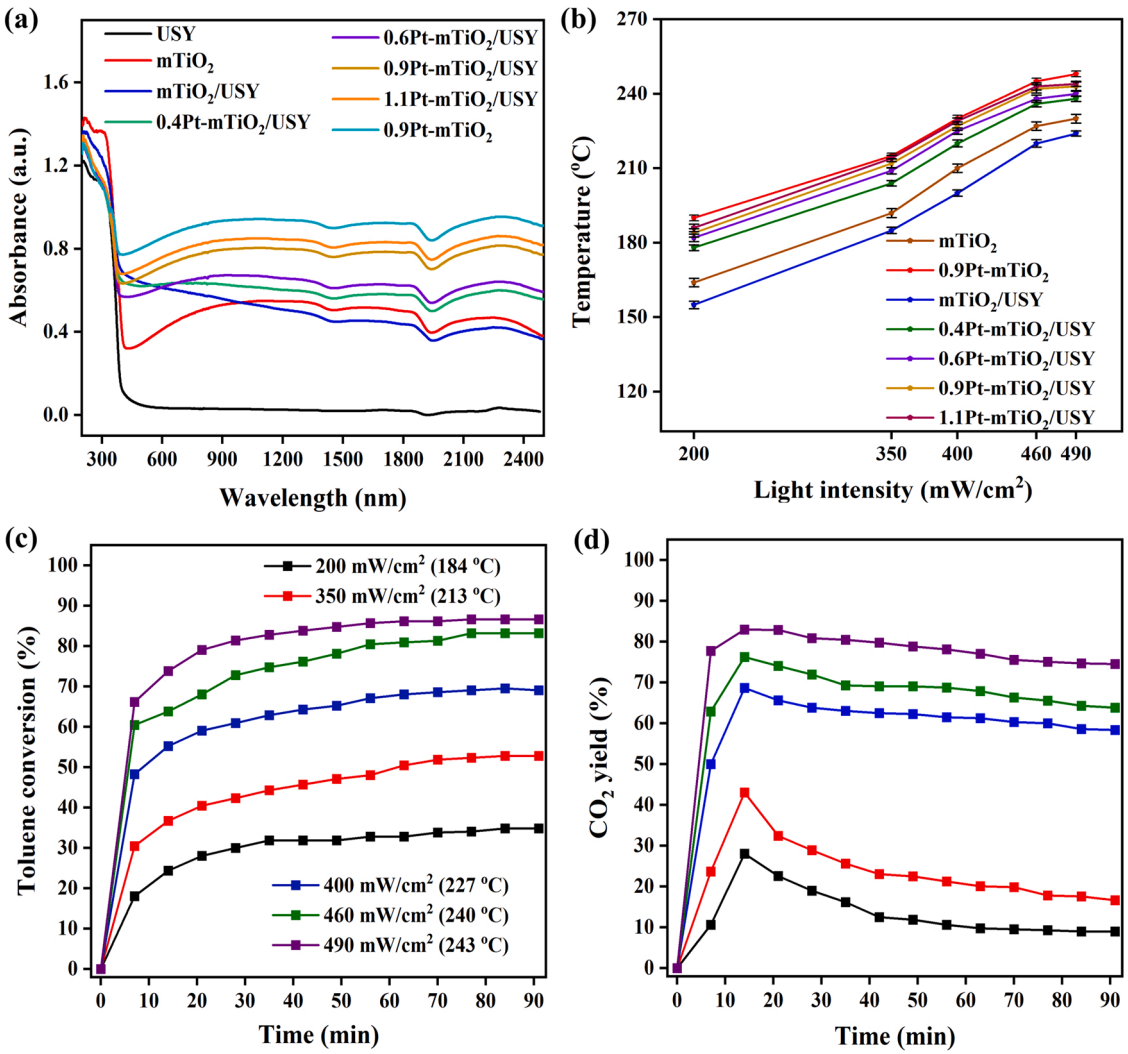

Fig. 6. UV–vis diffuse reflectance absorption spectra (a), equilibrium surface temperatures of the different catalyst samples under irradiation of different light intensities (The error bar represents the standard deviation of three evaluations) (b), toluene conversion (c) and CO_2 yield (d) over 0.9Pt-mTiO$_2$/USY under the irradiation of simulated sunlight with different intensities (200 ppm, 5 vol.% H_2O and WHSV = 26,000 mL g^{-1} h^{-1}).

Typically, the UV and part of the visible light are the sources of high photon energy to excite photocatalytic activity of semiconductors whereas the IR light often contributes to the catalytic reaction via the strong thermal effect. To understand how the light region affects the catalytic oxidation of toluene, the catalytic activities over 0.9Pt-mTiO$_2$/USY were carried out under the controlled conditions. The same reaction temperature over 0.9Pt-mTiO$_2$/USY was regulated by irradiation of full solar spectrum, UV–vis, or IR irradiation. As depicted in Fig. 7, under UV–vis light irradiation (240 °C), the toluene conversion and CO_2 yield reach 95% and 83%, respectively, exceeding that of the full solar spectrum (UV–vis–IR) at the same temperature. The excitation of semiconductor materials under IR light is difficult, notwithstanding, under IR irradiation, the toluene conversion and CO_2 yield reach 84.3% and 65.6% over 0.9Pt-mTiO$_2$/USY, respectively, which is slightly lower than that of the full solar spectrum at the same temperature. This result suggests that thermal energy is necessary to trigger the oxidation of toluene over 0.9Pt-mTiO$_2$/USY whilst the UV–vis light has a promotional effect on the oxidation reaction of toluene. In order to verify the possible contribution of photocatalysis during the reaction, the low-temperature catalytic activity on 0.9Pt-mTiO$_2$/USY under solar light irradiation with 460 mW/cm^2 of light intensity was performed by controlling the surface temperature of the catalyst layer at 30 °C through a cooling circulating pump containing water-glycol mixed solvent. It was found that there is an extremely low photocatalytic activity with ca. 9.7% of toluene conversion and ca. 1.3% of CO_2 yield (Fig. 7 **and S7**). The results also evidence that the catalytic activity is largely attributed to the high surface temperature of the catalyst layer driven by light. EPR signals (Fig. S8) of active •OH and $\bullet O_2^-$ radicals on 0.9Pt-mTiO$_2$/USY under light irradiation of 460 mW/cm^2 indicate that photocatalytic reaction associated with photogenerated charge carriers participates in toluene oxidation, but it doesn't actively contribute to the degradation of toluene under these reaction conditions (Rapid deactivation in catalytic activity is observed within 90 mins under the same conditions, as shown in Fig. S4). The above experimental results are in good agreement with the previous studies, which confirm that light-to-heat energy is crucial to activate and decompose toluene [5,6,15,45]. As a comparison, toluene degradation behavior over 0.9Pt-mTiO$_2$/USY under electric heating conditions was investigated at 240 °C (Fig. 7). Remarkably, its catalytic performance is lower than that under irradiation with a light intensity of 460 mW/cm^2 (240 °C). It suggests that light plays an additional role during the reaction apart from acting as a source of thermal energy.

3.4. Activation of lattice oxygen

The enhanced oxygen absorption and mobility property driven by

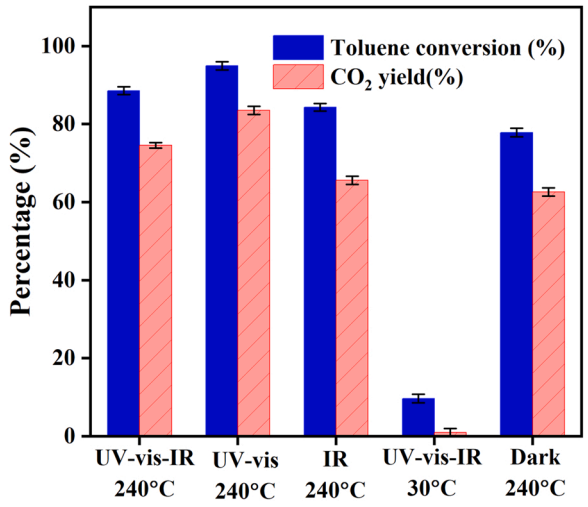

Fig. 7. Toluene conversion and CO_2 yield on 0.9Pt-mTiO_2/USY under the light irradiation of UV–vis–IR (abbreviated as UV–vis–IR, 240 °C), UV–vis at the same temperature (abbreviated as UV–vis, 240 °C), IR at the same temperature (abbreviated as IR, 240 °C), UV–vis -IR at 30 °C (abbreviated as UV–vis–IR, 30 °C) and in the dark at 240 °C (electric heating). The error bar represents the standard deviation of three evaluations.

the incorporation of Pt nanoparticles and USY support was reflected by O_2-TPD profiles, as shown in Fig. 8**a**. According to the previous reports, the peaks observed below 300 °C, 300–500 °C, and above 500 °C correspond to the physically absorbed oxygen, chemically absorbed oxygen, and lattice oxygen, respectively[46]. The mTiO_2 displayed only one peak at 770 °C, which can be ascribed to the bulk lattice oxygen. The addition of Pt nanoparticles resulted in the appearance of a broad peak at 143 °C and 309 °C suggesting that Pt nanoparticles improved the oxygen adsorption capacity and surface lattice oxygen migration ability [47]. The 0.9Pt-mTiO_2/USY, which possessed higher $O_{ads}/(O_{latt}+OH_2O)$ as displayed in Table 1, exhibited more intense desorption peaks and lower desorption temperatures at 231 °C, 643 °C, and 799 °C compared to mTiO_2/USY. This can be ascribed to the enhanced surface covalent metal-oxygen bond and electron affinity of oxygen vacant sites, due to the addition of Pt nanoparticles[48].

To get further insight into the other functions of light, low-temperature EPR under irradiation and in dark, O_2-TPD and toluene-TPD experiments with or without light pretreatment were performed. As shown in Fig. 8**b**, both mTiO_2/USY and 0.9Pt-mTiO_2/USY displayed two obvious signals at $g = 1.981$ and 2.004 assigned to Ti^{3+} and OVs in dark, respectively [49]. The EPR signal for the mTiO_2/USY appeared weaker in dark and under irradiation when compared to the 0.9Pt-mTiO_2/USY sample. This strongly indicates that more surface defects centers were formed after the introduction of Pt nanoparticles to mTiO_2/USY nanocomposite. The concentration of OVs on the surface of the catalyst is significant to enhancement for the adsorption of reactants. Under simulated solar irradiation, the EPR signal of mTiO_2/USY and 0.9Pt-mTiO_2/USY strengthened, indicating the promotional effect of light in the formation of OVs.

The O_2-TPD profiles of mTiO_2/USY and 0.9Pt-mTiO_2/USY with or without light pretreatment further addressed the additional role of light (Fig. 8**c**). With light pretreatment, the amount of oxygen desorption on mTiO_2/USY and 0.9Pt-mTiO_2/USY is much more than that without light

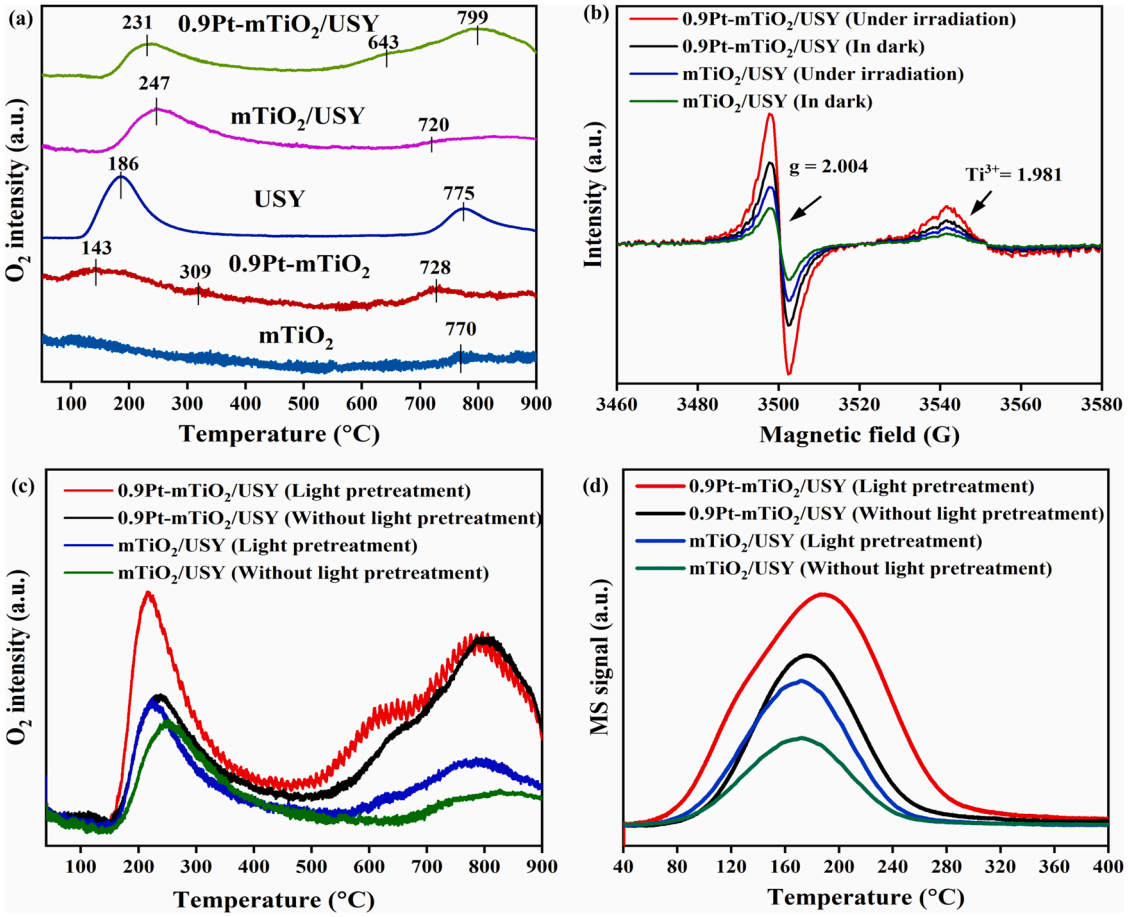

Fig. 8. (a) O_2-TPD curves of mTiO_2, 0.9Pt-mTiO_2, USY, mTiO_2/USY and 0.9Pt-mTiO_2/USY, EPR spectra recorded at 77 K (b), O_2-TPD curves (c) and toluene-TPD (d) of mTiO_2/USY and 0.9Pt-mTiO_2/USY with light pretreatment and without light pretreatment.

pretreatment, which might be due to the presence of more OVs verified by EPR analysis. OVs are directly associated with the generation of surface adsorbed oxygen species and serve as the reactive site for toluene oxidation. The intensity of physically and chemically absorbed oxygen below 300 °C are enhanced when samples were pretreated under light illumination compared to samples without light pretreatment. The O_2-TPD data with light pretreatment show desorption of more adsorbed oxygen in the low-temperature zone, which indicates a stronger oxygen absorption ability. The oxygen desorption intensity from the labile surface lattice oxygen in the temperature range between 300 and 500 °C slightly increased. The desorption of oxygen at temperatures above 500 °C is associated with bulk lattice oxygen. The presence of abundant OVs and promotional activation of the lattice oxygen under irradiation boosts the catalytic activity of the 0.9Pt-mTiO_2/USY nanocomposite. Thus, light is not a source of thermal energy for toluene oxidation but also facilitates more active oxygen generation to participate in the oxidation reaction. The toluene adsorption is significantly enhanced after light pretreatment as depicted in Fig. 8**d.** The 0.9Pt-mTiO_2/USY displays the strongest affinity to toluene molecules after light pretreatment. Based on the above observation, light-driven photothermocatalytic oxidation of toluene over 0.9Pt-mTiO_2/USY is triggered by thermocatalysis associated with photoactivation.

To investigate the contribution of the different light regions towards promoting lattice oxygen activation, EPR, O_2-TPD, and toluene-TPD analyses were carried out over 0.9Pt-mTiO_2/USY by filtering UV–vis or IR irradiation (Fig. 9). The EPR signal for the 0.9Pt-mTiO_2/USY sample appeared higher under UV–vis irradiation compared to IR irradiation. The intensity of physically and chemically absorbed oxygen below 300 °C increased after UV–vis light pretreatment compared to the signal after IR light pretreatment. Besides, UV–vis light has a strong promoting effect on the catalytic reaction (Fig. 7). The toluene adsorption heightens under UV–vis light compared to the IR light which further establishes the role of the UV-Vis region in the activation of lattice oxygen.

Several studies have reported that the presence of OVs on the surface of metal oxide enhances the electrostatic adsorption of toluene due to the change in surface charge distribution [43]. The addition of Pt nanoparticles increases the amount of oxygen vacancies which act as an electron donor for the effective adsorption and activation of molecular oxygen [50]. The DFT calculation of oxygen vacancy formation energy (E_{OV}) can be implored to measure the energy used to create an oxygen defect. The oxygen vacancy formation energy of TiO_2 and TiO_2-Pt was calculated by the Eq. (4):

$$\Delta E = E_{OV} + \quad 1/2E_{O_2} - E_{perfect} \tag{4}$$

E_{OV} represents the energy of the model with an oxygen vacancy defect, $E_{perfect}$ represents the energy of the model without any defect.

Theoretical results suggest that the oxygen vacancy formation energy for anatase TiO_2 is 3.44 eV, and the loading of Pt nanoparticles into the perfect Pt-TiO_2 **(**Fig. S9**)** decreases the formation energy to 1.64 eV and 1.60 eV for a single and double oxygen vacant point, respectively **(**Fig. 10**).** The results confirm that the introduction of Pt nanoparticles favors the formation of oxygen vacancies, which agrees with the O 1 s XPS spectra **(**Fig. 3**b)** and EPR results **(**Fig. 8**b).**

3.5. Reaction pathway

In situ DRIFTS analysis was employed to study the role of lattice oxygen in light-driven thermocatalysis for toluene oxidation on 0.9Pt-mTiO_2/USY, as shown in Fig. 11 **(a-d)**. Before starting experiments, all catalysts were thermally pretreated at 350 °C in He to remove surface adsorbed oxygen species and then cooled to room temperature. Afterward, 200 ppm toluene/He was introduced to the cell with a flow rate of 20 mL/min at room temperature. As described in Fig. 11**a**, the characteristic peaks of adsorbed toluene are gradually intensified within 10 mins, where the peaks at around 1600, 1495, 1395 cm^{-1} can be attributed to the stretching vibration of the toluene aromatic ring and the peaks in the range of 2868–3487 cm^{-1} are related to adsorbed toluene on the surface of the catalyst. The temperature of the IR cell was increased to 150 °C in He flow without irradiation. With reaction time, it can be observed that is a slight change in the peaks of toluene as well as the appearance of several small peaks, indicating the transformation of toluene to intermediates **(**Fig. 11**b).** The increased peaks at 2879, 2927, and 3027 cm^{-1} are attributed to the asymmetric/symmetric stretching of aliphatic groups resulting from the breaking or activating of the CH_3 group of the aromatic ring and a new broad peak centered at 1640 cm^{-1} is from benzaldehyde as the oxidized intermediate. In the absence of reactant oxygen molecules, only a small amount of surface-active lattice oxygen and OVs play an active role in the toluene activation and intermediates formation [14]. In Fig. 11**c**, the characteristics peaks of intermediates including benzaldehyde (1653 and 1646 cm^{-1}), benzoic acid (1600–1800 cm^{-1}), carboxylate (1540 and 1520 cm^{-1}) are noticeably heightened with the introduction of light irradiation (460 mW/cm^2) at the same conditions (150 °C and He flow) with reaction time [7]. The identification of these characteristic peaks of important intermediates demonstrates that toluene oxidation over 0.9Pt-mTiO_2/USY can proceed by utilizing surface−active lattice oxygen of catalyst in absence of gaseous oxygen. It also verifies that the existence of photoactivation to stimulate more surface lattice oxygen to take part in the toluene oxidation reaction on 0.9Pt-mTiO_2/USY. In the absence of external oxygen supplements, it is difficult to provide more active lattice oxygen to participate in the oxidation of toluene, therefore O_2 was introduced into the IR cell. With the introduction of O_2 into the IR cell, consumed surface active oxygen can be replenished to maintain

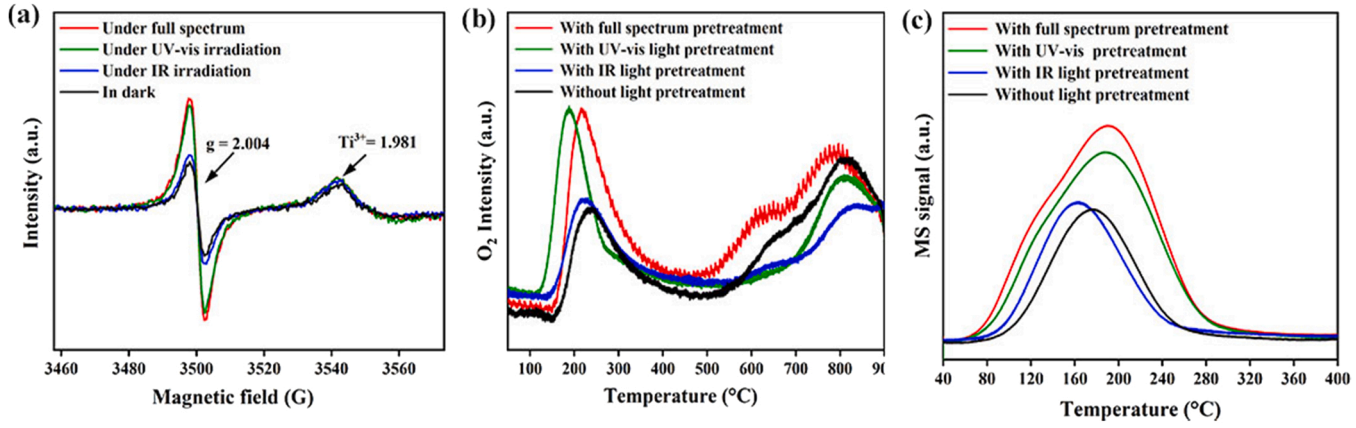

Fig. 9. (a) EPR spectra recorded at 77 K (b), O_2-TPD curves (c) and toluene-TPD (d) of 0.9Pt-mTiO_2/USY after different light pretreatment.

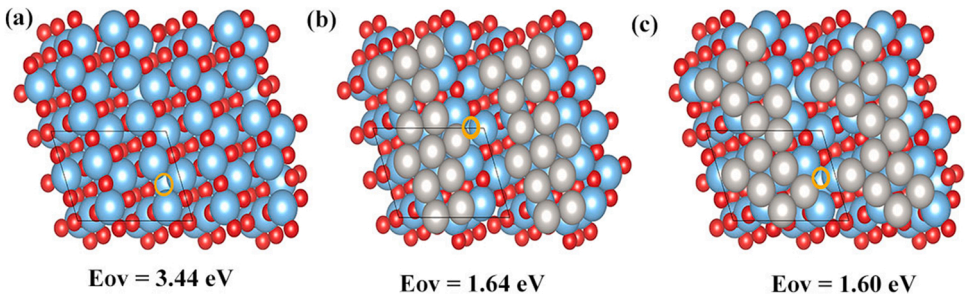

Fig. 10. Formation energy of a single oxygen vacancy over perfect anatase TiO_2(a) and Pt-TiO_2 (b-c).

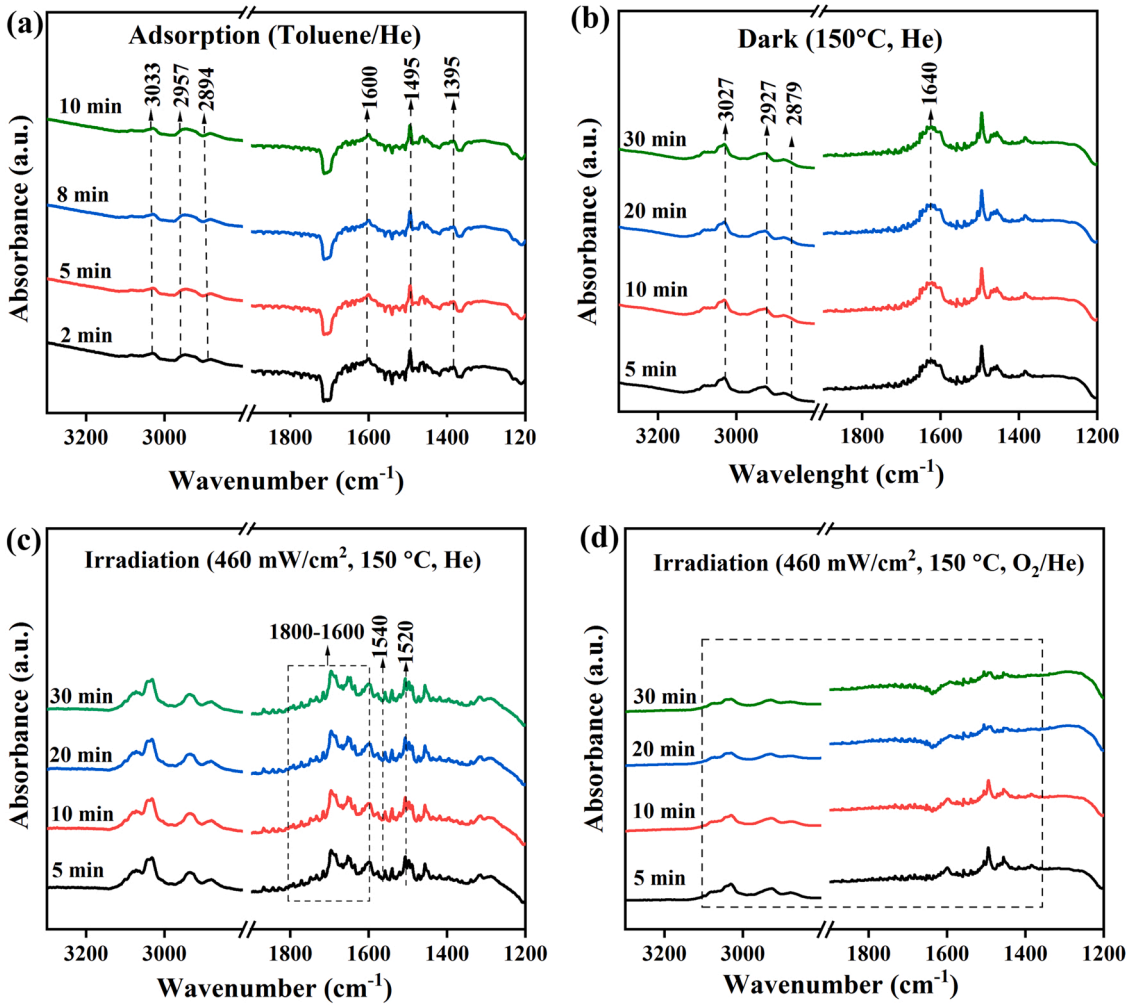

Fig. 11. In situ DRIFTS spectra of toluene degradation over 0.9Pt-mTiO_2/USY ((a) absorption under toluene/He flow, (b) reaction in dark at 150 °C under He flow, (c) reaction under light irradiation of 460 mW/cm^2 at 150 °C under He flow, (d) reaction under light irradiation of 460 mW/cm^2 at 150 °C under O_2/He flow).

the process of oxidation and accelerate the mineralization of toluene and intermediates [7]. As depicted in Fig. 11**d**, the peaks of intermediates almost disappear within 30 mins. Based on the aforementioned results and analyses, the possible reaction pathway is obeyed as follows: toluene → benzaldehyde → benzoic acid → maleic anhydride → CO_2 and H_2O, as illustrated in Fig. 12. The obtained results reveal that the reaction is consistent with the Mars-van Krevelen mechanism, and Ti^{3+}, OVs, and Pt species play an indispensable role in the light-driven thermocatalysis of toluene oxidation [9]. have been reported to facilitate the formation of carboxylates whereas OVs promotes the aromantic ring-opening of the adsorbed toluene [11]. The Ti^{3+}, OVs, and Pt NPs collectively harvest light to provide thermal energy for the oxidative reaction. Moreover, light irradiation promotes the activation of oxygen species that further enhanced lattice oxygen mobility and gaseous oxygen activation to form benzaldehyde, benzoic acid, benzoate species, and finally H_2O and CO_2.

3.6. *Stability of catalytic performance and catalyst structure*

The 0.9Pt-mTiO_2/USY catalyst exhibits excellent durability for the light-driven thermal oxidation of toluene under the irradiation of simulated sunlight with a light intensity of 490 mW/cm^2 under humid conditions (Fig. 13**a**). The light-driven catalytic performance can effectively maintain the almost same removal efficiency (ca. 86% of

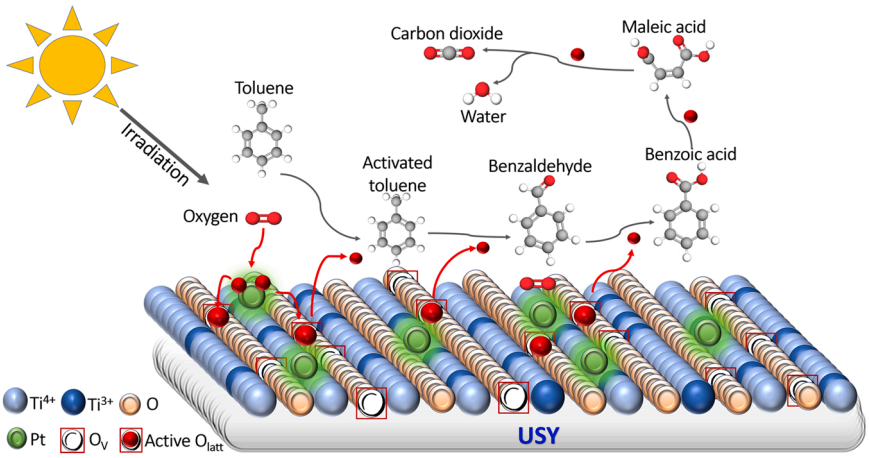

Fig. 12. Scheme of toluene oxidation over 0.9Pt-mTiO$_2$/USY.

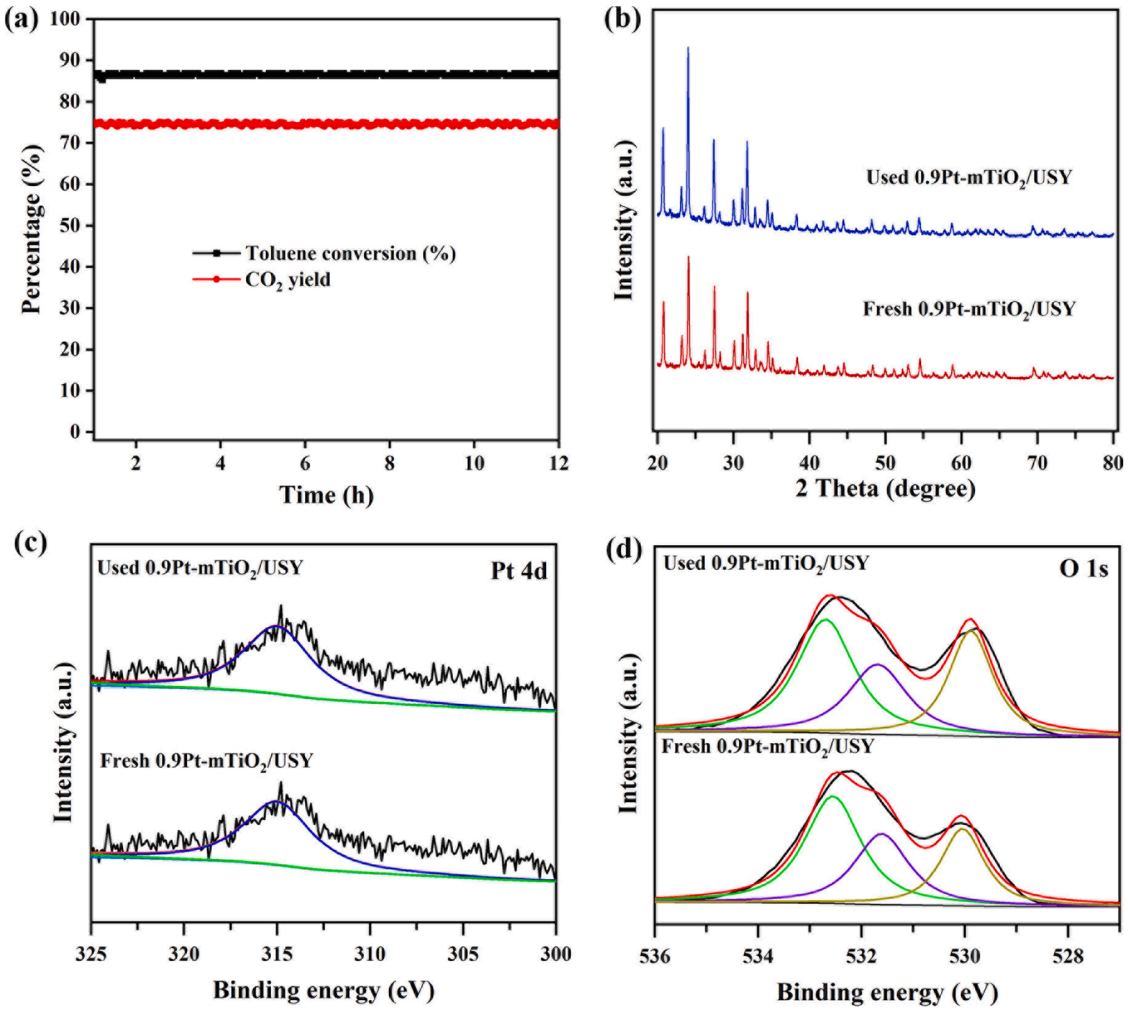

Fig. 13. Durability of 0.9Pt-mTiO$_2$/USY under irradiation of 490 mW/ cm^2 simulated sunlight (a), XRD patterns (b), Pt 4d XPS spectra (c) and O1s XPS spectra (d) of the fresh and used 0.9Pt-mTiO$_2$/USY.

toluene conversion and ca. 74% of CO_2 yield) after continuous irradiation for 12 h. The synergistic contribution of the hydrophobic USY support and highly efficient conversion of light-to-heat effectively promotes the catalyst performance under humid conditions. As shown in Fig. 13**b**, the XRD result for used 0.9Pt-mTiO$_2$/USY almost remains unaltered, suggesting its good structure stability. The USY support provides sufficient surface area and abundant active sites to limit the phase transformation of metallic Pt to less-reactive Pt oxide, as verified by XPS (Fig. 13**c**) [23]. There is no significant difference between the binding energies of the fresh and used samples (Fig. 13**c,d**), indicating the good stability of the catalyst. Thus, it suggests that 0.9Pt-mTiO$_2$/USY keeps good catalytic durability and structural stability in the

light-driven thermocatalysis.

To further explore the practical application of 0.9Pt-mTiO$_2$/USY under solar light irradiation at 240 °C, the mineralization of various VOCs such as formaldehyde, benzene, and ethyl acetate with an initial concentration of 500, 150 and 108 ppm were investigated with a feed gas containing 5% vol. water vapor. **(**Fig. S10**).** The 0.9Pt-mTiO$_2$/USY exhibited photothermocatalytic activity for benzene and ethyl acetate oxidation under the same light intensity of 490 mW/cm^2 and reaction temperature of 240 °C as presented in Fig. S10. The activities of 0.9Pt-mTiO$_2$/USY for benzene catalytic oxidation were even higher than ethyl acetate, which might be due to that the microporous characteristic of the USY zeolite limits the adsorption of large molecule size, into the pore channels of zeolites[23]. The formaldehyde was completely oxidized at 60 °C under a light intensity of 50 mW/cm^2. This result indicates the mineralization efficiency and wide VOCs purification applicability of the 0.9Pt-mTiO$_2$/USY composite.

4. Conclusions

In summary, the utilization of renewable solar energy via light-driven thermocatalysis offers a potential alternative strategy for VOCs remediation. The Pt-mTiO$_2$/USY nanocomposites show efficient light utilization due to their strong absorption in the full solar spectrum and high solar heating effect. More importantly, the catalytic activity of 0.9Pt-mTiO$_2$/USY remained stable under humid conditions, demonstrating its high durability for the oxidation of toluene. The introduction of Pt NPs on mTiO$_2$/USY enhanced the light absorption ability of the catalyst and causes the formation of more OVs and Ti^{3+} species. The large specific surface area of USY makes Pt species solidly uniform dispersion on support, and abundant channels are in favor of diffusion and activation of toluene molecules in the reaction. The strong synergistic effect of Ti^{3+}, OVs, and Pt NPs harvests light to provide thermal energy for the oxidative reaction and offers active sites for activation and deep dissociation of toluene. Light not only contributes as a source of thermal energy but also promotes the photoactivation of more active lattice oxygen in the reaction process. Therefore, the oxidation of toluene on 0.9Pt-mTiO$_2$/USY is light-driven thermocatalysis accompanied by the photoactivation of surface oxygen species. This study highlights the potential of zeolite-based nanocomposites with multiple reactive sites for enhanced utilization of solar energy for the mineralization of VOCs.

CRediT authorship contribution statement

Ehiaghe Agbovhimen Elimian: Conceptualization, Methodology, Investigation, Data curation, Formal analysis, Writing - original draft. **Meng Zhang**: Methodology, Investigation, Data curation, Formal analysis. **Jing Chen**: Conceptualization, Writing - review & editing. **Hongpeng Jia**: Conceptualization, Supervision, Writing - review & editing, Project administration, Funding acquisition. **Yong Sun and Jun He**: Methodology.

Declaration of Competing Interest

The authors declare that they have no known competing financial interests or personal relationships that could have appeared to influence the work reported in this paper.

Acknowledgments

This work was supported by the Strategic Priority Research Program of the Chinese Academy of Sciences [No. XDPB1902]; the National Natural Science Foundation of China [No. 21976172]; the Science and Technology Planning Project of Fujian Province [2020Y0084]; the Youth Innovation Promotion Association of CAS [No. 2021304]; the FJIRSM&IUE Joint Research Fund [No. RHZX-2019-007].

Appendix A. Supporting information

Supplementary data associated with this article can be found in the online version at doi:10.1016/j.apcatb.2022.121203.

References

[1] J.J. Li, S.C. Cai, Z. Xu, X. Chen, J. Chen, H.P. Jia, J. Chen, Solvothermal syntheses of Bi and Zn co-doped TiO$_2$ with enhanced electron-hole separation and efficient photodegradation of gaseous toluene under visible-light, J. Hazard. Mater. (2017), https://doi.org/10.1016/j.jhazmat.2016.12.004.

[2] S. Mo, Q. Zhang, J. Li, Y. Sun, Q. Ren, S. Zou, Q. Zhang, J. Lu, M. Fu, D. Mo, J. Wu, H. Huang, D. Ye, Highly efficient mesoporous MnO$_2$ catalysts for the total toluene oxidation: oxygen-Vacancy defect engineering and involved intermediates using in situ DRIFTS, Appl. Catal. B Environ. 264 (2020), 118464, https://doi.org/10.1016/j.apcatb.2019.118464.

[3] T. Guo, Z. Bai, C. Wu, T. Zhu, Influence of relative humidity on the photocatalytic oxidation (PCO) of toluene by TiO$_2$ loaded on activated carbon fibers: PCO rate and intermediates accumulation, Appl. Catal. B Environ. 79 (2008) 171–178, https://doi.org/10.1016/j.apcatb.2007.09.033.

[4] T. Xu, H. Zheng, P. Zhang, Isolated Pt single atomic sites anchored on nanoporous TiO$_2$ film for highly efficient photocatalytic degradation of low concentration toluene, J. Hazard. Mater. 388 (2020), 121746, https://doi.org/10.1016/j.jhazmat.2019.121746.

[5] J. Li, M. Zhang, E.A. Elimian, X. Lv, J. Chen, H. Jia, Convergent ambient sunlight-powered multifunctional catalysis for toluene abatement over in situ exsolution of Mn$_3$O$_4$ on perovskite parent, Chem. Eng. J. 412 (2021), 128560, https://doi.org/10.1016/j.cej.2021.128560.

[6] M. Zhang, S. Cai, J. Li, E.A. Elimian, J. Chen, H. Jia, Ternary multifunctional catalysts of polymeric carbon nitride coupled with Pt-embedded transition metal oxide to enhance light-driven photothermal catalytic degradation of VOCs, J. Hazard. Mater. 412 (2021), 125266, https://doi.org/10.1016/j.jhazmat.2021.125266.

[7] E. Yu, J. Li, J. Chen, J. Chen, Z. Hong, H. Jia, Enhanced photothermal catalytic degradation of toluene by loading Pt nanoparticles on manganese oxide: photoactivation of lattice oxygen, J. Hazard. Mater. 388 (2020), 121800, https://doi.org/10.1016/j.jhazmat.2019.121800.

[8] R. Qi, P. Yu, J. Zhang, W. Guo, Y. He, H. Hojo, H. Einaga, Q. Zhang, X. Liu, Z. Jiang, W. Shangguan, Efficient visible light photocatalysis enabled by the interaction between dual cooperative defect sites, Appl. Catal. B Environ. 274 (2020), 119099, https://doi.org/10.1016/j.apcatb.2020.119099.

[9] Q. Cheng, A. Wang, Z. Song, J. Bao, J. Xue, Y. Wei, S. Li, L. Lv, J. Ding, M. Cai, J. Chen, Q. Wang, C. Gao, S. Sun, Enhancement and stabilization of isolated hydroxyl groups via the construction of coordinatively unsaturated sites on surface and subsurface of hydrogenated TiO$_2$ nanotube arrays for photocatalytic complete mineralization of toluene, J. Environ. Chem. Eng. 9 (2021), 105080, https://doi.org/10.1016/j.jece.2021.105080.

[10] J. Kong, Z. Xiang, G. Li, T. An, Introduce oxygen vacancies into CeO$_2$ catalyst for enhanced coke resistance during photothermocatalytic oxidation of typical VOCs, Appl. Catal. B Environ. 269 (2020), 118755, https://doi.org/10.1016/j.apcatb.2020.118755.

[11] Q. Wu, J. Ye, W. Qiao, Y. Li, J.W. (Hans) Niemantsverdriet, E. Richards, F. Pan, R. Su, Inhibit the formation of toxic methylphenolic by-products in photo-decomposition of formaldehyde–toluene/xylene mixtures by Pd cocatalyst on TiO$_2$, Appl. Catal. B Environ. 291 (2021), 120118, https://doi.org/10.1016/j.apcatb.2021.120118.

[12] J. Hu, X. Gao, Q. Fan, X. Gao, Facial controlled synthesis of Pt/MnO$_2$ catalysts with high efficiency for VOCs combustion, RSC Adv. 11 (2021) 16547–16556, https://doi.org/10.1039/D1RA02112E.

[13] D. Yang, S. Fu, S. Huang, W. Deng, Y. Wang, L. Guo, T. Ishihara, The preparation of hierarchical Pt/ZSM-5 catalysts and their performance for toluene catalytic combustion, Microporous Mesoporous Mater. 296 (2020), 109802, https://doi.org/10.1016/j.micromeso.2019.109802.

[14] J.J. Li, S.C. Cai, E.Q. Yu, B. Weng, X. Chen, J. Chen, H.P. Jia, Y.J. Xu, Efficient infrared light promoted degradation of volatile organic compounds over photo-thermal responsive Pt-rGO-TiO$_2$ composites, Appl. Catal. B Environ. 233 (2018) 260–271, https://doi.org/10.1016/j.apcatb.2018.04.011.

[15] J.J. Li, S.C. Cai, X. Chen, D.X. Yan, J. Chen, H.P. Jia, Engineering rGO nanosheets-adsorption layer supported Pt nanoparticles to enhance photo- thermal catalytic activity under light irradiation, J. Mater. Chem. A 7 (2019) 11985–11995, https://doi.org/10.1039/c9ta00148d.

[16] E.J. Radich, A.L. Krenselewski, J. Zhu, P.V. Kamat, Is graphene a stable platform for photocatalysis? Mineralization of reduced graphene oxide with UV-irradiated TiO2 nanoparticles, Chem. Mater. 26 (2014) 4662–4668, https://doi.org/10.1021/cm5026552.

[17] C.R. Minitha, V.S. Anithaa, V. Subramaniam, R.T. Rajendra Kumar, Impact of oxygen functional groups on reduced graphene oxide-based sensors for ammonia and toluene detection at room temperature, ACS Omega 3 (2018) 4105–4112, https://doi.org/10.1021/acsomega.7b02085.

[18] M. Takeuchi, M. Hidaka, M. Anpo, Efficient removal of toluene and benzene in gas phase by the TiO$_2$/Y-zeolite hybrid photocatalyst, J. Hazard. Mater. 237–238 (2012) 133–139, https://doi.org/10.1016/j.jhazmat.2012.08.011.

[19] J. Fernández-Catalá, M. Sánchez-Rubio, M. Navlani-García, Á. Berenguer-Murcia, D. Cazorla-Amorós, Synthesis of TiO$_2$/nanozeolite composites for highly efficient

photocatalytic oxidation of propene in the gas phase, ACS Omega 5 (2020) 31323–31331, https://doi.org/10.1021/acsomega.0c04793.
[20] P.K. Dutta, M. Severance, Photoelectron transfer in zeolite cages and its relevance to solar energy conversion, J. Phys. Chem. Lett. 2 (2011) 467–476, https://doi.org/10.1021/jz101500z.
[21] Y. Zhao, W. Gao, S. Li, G.R. Williams, A.H. Mahadi, D. Ma, Solar- versus thermal-driven catalysis for energy conversion, Joule 3 (2019) 920–937, https://doi.org/10.1016/j.joule.2019.03.003.
[22] M. Kraus, U. Trommler, F. Holzer, F.D. Kopinke, U. Roland, Competing adsorption of toluene and water on various zeolites, Chem. Eng. J. 351 (2018) 356–363, https://doi.org/10.1016/j.cej.2018.06.128.
[23] Y. Shi, Z. Li, J. Wang, R. Zhou, Synergistic effect of Pt/Ce and USY zeolite in Pt-based catalysts with high activity for VOCs degradation, Appl. Catal. B Environ. 286 (2021), 119936, https://doi.org/10.1016/j.apcatb.2021.119936.
[24] B.Y. Guan, L. Yu, J. Li, X.W. Lou, A universal cooperative assembly-directed method for coating of mesoporous TiO_2 nanoshells with enhanced lithium storage properties, Sci. Adv. 2 (2016) 2–10, https://doi.org/10.1126/sciadv.1501554.
[25] P. Wang, D. Wang, H. Li, T. Xie, H. Wang, Z. Du, A facile solution-phase synthesis of high quality water-soluble anatase TiO_2 nanocrystals, J. Colloid Interface Sci. 314 (2007) 337–340, https://doi.org/10.1016/j.jcis.2007.05.087.
[26] B. Chakraborty, I.A. Weinstock, Water-soluble titanium-oxides: complexes, clusters and nanocrystals, Coord. Chem. Rev (2019) 85–102, https://doi.org/10.1016/j.ccr.2018.11.011.
[27] M. Fathy, H. Hamad, A.E.H. Kashyout, Influence of calcination temperatures on the formation of anatase TiO_2 nano rods with a polyol-mediated solvothermal method, RSC Adv. 6 (2016) 7310–7316, https://doi.org/10.1039/C5RA26739K.
[28] J.F. Lambert, E. Marceau, B. Shelimov, J. Lehman, V. Le Bel de Penguilly, X. Carrier, S. Boujday, H. Pernot, M. Che, Thermal chemistry of oxide-supported platinum catalysts: a comparative study, in: A. Corma, F.V. Melo, S. Mendioroz, J. L.G.B.T.-S. in S.S., C. Fierro (Eds.), 12th Int. Congr. Catal., Elsevier, 2000, pp. 1043–1048, https://doi.org/10.1016/S0167-2991(00)80336-5.
[30] H. Deng, T. Pan, Y. Zhang, L. Wang, Q. Wu, J. Ma, W. Shan, H. He, Adsorptive removal of toluene and dichloromethane from humid exhaust on MFI, BEA and FAU zeolites: an experimental and theoretical study, Chem. Eng. J. 394 (2020), 124986, https://doi.org/10.1016/j.cej.2020.124986.
[31] W.-K. Wang, J.-J. Chen, X. Zhang, Y.-X. Huang, W.-W. Li, H.-Q. Yu, Self-induced synthesis of phase-junction TiO_2 with a tailored rutile to anatase ratio below phase transition temperature, Sci. Rep. 6 (2016) 20491, https://doi.org/10.1038/srep20491.
[32] S. Besselmann, E. Löffler, M. Muhler, On the role of monomeric vanadyl species in toluene adsorption and oxidation on V_2O_5/TiO_2 catalysts: a Raman and in situ DRIFTS study, J. Mol. Catal. A Chem. 162 (2000) 401–411, https://doi.org/10.1016/S1381-1169(00)00307-1.
[33] D. Yan, Q. Li, H. Zhang, X. Zhou, H. Chen, A highly dispersed mesoporous zeolite@TiO_2 – supported Pt for enhanced sulfur-resistance catalytic CO oxidation, Catal. Commun. 142 (2020), 106042, https://doi.org/10.1016/j.catcom.2020.106042.
[34] M. Hu, Z. Xing, Y. Cao, Z. Li, X. Yan, Z. Xiu, T. Zhao, S. Yang, W. Zhou, Ti3+ self-doped mesoporous black $TiO_2/SiO_2/g\text{-}C_3N_4$ sheets heterojunctions as remarkable visible-lightdriven photocatalysts, Appl. Catal. B Environ. 226 (2018) 499–508, https://doi.org/10.1016/j.apcatb.2017.12.069.
[35] H. Peng, T. Dong, L. Zhang, C. Wang, W. Liu, J. Bao, X. Wang, N. Zhang, Z. Wang, P. Wu, P. Zhang, S. Dai, Active and stable Pt-Ceria nanowires@silica shell catalyst: design, formation mechanism and total oxidation of CO and toluene, Appl. Catal. B Environ. 256 (2019), 117807, https://doi.org/10.1016/j.apcatb.2019.117807.
[36] L.-Y. Lin, S. Kavadiya, X. He, W.-N. Wang, B.B. Karakocak, Y.-C. Lin, M.Y. Berezin, P. Biswas, Engineering stable Pt nanoparticles and oxygen vacancies on defective TiO_2 via introducing strong electronic metal-support interaction for efficient CO_2 photoreduction, Chem. Eng. J. 389 (2020), 123450, https://doi.org/10.1016/j.cej.2019.123450.
[37] Y. Cao, Z. Xing, Y. Shen, Z. Li, X. Wu, X. Yan, J. Zou, S. Yang, W. Zhou, Mesoporous black Ti^{3+}/N-TiO_2 spheres for efficient visible-light-driven photocatalytic performance, Chem. Eng. J. 325 (2017) 199–207, https://doi.org/10.1016/j.cej.2017.05.080.
[38] S.C. Cai, J.J. Li, E.Q. Yu, X. Chen, J. Chen, H.P. Jia, Strong photothermal effect of plasmonic Pt nanoparticles for efficient degradation of volatile organic compounds under solar light irradiation, ACS Appl. Nano Mater. 1 (2018) 6368–6377, https://doi.org/10.1021/acsanm.8b01578.
[39] H. Huang, J. Feng, S. Zhang, H. Zhang, X. Wang, T. Yu, C. Chen, Z. Yi, J. Ye, Z. Li, Z. Zou, Molecular-level understanding of the deactivation pathways during methanol photo-reforming on Pt-decorated TiO_2, Appl. Catal. B Environ. 272 (2020), 118980, https://doi.org/10.1016/j.apcatb.2020.118980.
[40] T. Yin, X. Meng, L. Jin, C. Yang, N. Liu, L. Shi, Prepared hydrophobic Y zeolite for adsorbing toluene in humid environment, Microporous Mesoporous Mater. 305 (2020), 110327, https://doi.org/10.1016/j.micromeso.2020.110327.
[41] Y. Zhang, Z. Si, J. Gao, Y. Liu, L. Liu, X. Wu, R. Ran, D. Weng, Facile synthesis of NaOH-promoted Pt/TiO_2 catalysts for toluene oxidation under visible light irradiation, Appl. Surf. Sci. 469 (2019) 246–252, https://doi.org/10.1016/j.apsusc.2018.11.060.
[42] T. Gan, X. Chu, H. Qi, W. Zhang, Y. Zou, W. Yan, G. Liu, Pt/Al_2O_3 with ultralow Pt-loading catalyze toluene oxidation: promotional synergistic effect of Pt nanoparticles and Al_2O_3 support, Appl. Catal. B Environ. 257 (2019), 117943, https://doi.org/10.1016/j.apcatb.2019.117943.
[43] X. Yang, X. Yu, M. Jing, W. Song, J. Liu, M. Ge, Defective $MnxZr_{1-x}O_2$ solid solution for the catalytic oxidation of toluene: insights into the oxygen vacancy contribution, ACS Appl. Mater. Interfaces 11 (2019) 730–739, https://doi.org/10.1021/acsami.8b17062.
[44] H. Liu, H. Fu, Y. Liu, X. Chen, K. Yu, L. Wang, Synthesis, characterization and utilization of oxygen vacancy contained metal oxide semiconductors for energy and environmental catalysis, Chemosphere 272 (2021), 129534, https://doi.org/10.1016/j.chemosphere.2021.129534.
[45] X. Chen, S. Cai, E. Yu, J. Li, J. Chen, H. Jia, Photothermocatalytic performance of ACo_2O_4 type spinel with light-enhanced mobilizable active oxygen species for toluene oxidation, Appl. Surf. Sci. 484 (2019) 479–488, https://doi.org/10.1016/j.apsusc.2019.04.093.
[46] H. Shang, M. Li, H. Li, S. Huang, C. Mao, Z. Ai, L. Zhang, Oxygen vacancies promoted the selective photocatalytic removal of NO with blue TiO_2 via simultaneous molecular oxygen activation and photogenerated hole annihilation, Environ. Sci. Technol. 53 (2019) 6444–6453, https://doi.org/10.1021/acs.est.8b07322.
[47] J. Chen, M. Jiang, W. Xu, J. Chen, Z. Hong, H. Jia, Incorporating Mn cation as anchor to atomically disperse Pt on TiO_2 for low-temperature removal of formaldehyde, Appl. Catal. B Environ. 259 (2019), 118013, https://doi.org/10.1016/j.apcatb.2019.118013.
[48] Z. Wu, Y. Li, W. Huang, Size-dependent Pt-TiO_2 strong metal–support interaction, J. Phys. Chem. Lett. 11 (2020) 4603–4607, https://doi.org/10.1021/acs.jpclett.0c01560.
[49] Z. Lian, W. Wang, G. Li, F. Tian, K.S. Schanze, H. Li, Pt-enhanced mesoporous Ti^{3+}/TiO_2 with rapid bulk to surface electron transfer for photocatalytic hydrogen evolution, ACS Appl. Mater. Interfaces 9 (2017) 16959–16966, https://doi.org/10.1021/acsami.6b11494.
[50] Y. Zeng, Y. Wang, Y. Meng, F. Song, S. Zhang, Q. Zhong, The effect of preparation method on oxygen activation over Pt/TiO_2 catalysts for toluene total oxidation, Chem. Phys. Lett. 730 (2019) 95–99, https://doi.org/10.1016/j.cplett.2019.05.048.